

# 3D High-Quality Magnetic Resonance Image Restoration in Clinics Using Deep Learning

Hao Li <sup>#</sup>, Jianan Liu <sup>#</sup>

arXiv:2111.14259v3 [eess.IV] 27 Jan 2022

**Abstract**— Shortening acquisition time and reducing the motion artifacts are two of the most essential concerns in magnetic resonance imaging. As a promising solution, deep learning-based high quality MR image restoration has been investigated to generate higher resolution and motion artifact-free MR images from lower resolution images acquired with shortened acquisition time or motion artifact-corrupted images, without costing additional acquisition time or modifying the pulse sequences. However, numerous problems still exist to prevent deep learning approaches from becoming practical in the clinic environment. Specifically, most of the prior works focus solely on the network model but ignore the impact of various downsampling strategies on the acquisition time. Besides, the long inference time and high GPU consumption are also the bottle neck to deploy most of the prior works in clinics. Furthermore, prior studies employ random movement in retrospective motion artifact generation, resulting in uncontrollable severity of motion artifact. More importantly, doctors are unsure whether the generated MR images are trustworthy, making diagnosis difficult. To overcome all these problems, we adopted a unified 2D deep learning neural network for both 3D MRI super resolution and motion artifact reduction, demonstrating such a framework can achieve better performance in 3D MRI restoration task compared to other states of the art methods and remains the GPU consumption and inference time significantly low, thus easier to deploy. We also analyzed several downsampling strategies based on the acceleration factor, including multiple combinations of in-plane and through-plane downsampling, and developed a controllable and quantifiable motion artifact generation method. At last, the pixel-wise uncertainty was calculated and used to estimate the accuracy of generated image, providing additional information for reliable diagnosis.

**Index Terms**— MRI, 3D Super Resolution, In-plane and Through-plane Downsampling Strategy, Motion Artifact Generation, 3D Motion-Artifact Reduction, Aleatoric and Epistemic Uncertainty, Deep Learning for Clinic.

## I. INTRODUCTION

MAGNETIC resonance imaging (MRI) is widely used in a wide range of medical applications to aid precise diagnosis. However, doctors are frequently confronted with the resolution-acquisition time trade-off in clinical environment, due to the capacity of hardware and the cooperation of patients.

<sup>#</sup> Hao Li and Jianan Liu contribute equally to the work and are co-first authors. Order is alphabetical.

Jianan Liu is with Vitalent Consulting, Gothenburg, Sweden.

Hao Li is with Department of Neuroradiology, University Hospital, Rupert-Karls-University Heidelberg, Heidelberg, Germany.

The acquisition of high resolution (HR) magnetic resonance images consumes more scan time, but the patients cannot remain still for such a long period, resulting in high probability of motion artifact. On the other hand, shortened acquisition time is more applicable for patients, whereas the images with sufficient resolution can hardly be obtained. Therefore, with the capability to recover the resolution loss of HR images from low resolution (LR) images and reduce the motion artifact, deep learning-based super resolution (SR) and motion artifact reduction (MAR) technique is a promising approach, as it reconstructs high quality images without extra scan time or any modification on the MR pulse sequence.

Super resolution image reconstruction, as one of the major fields of computer vision, was deeply influenced by deep learning technology. In such a data-driven approach, a large number of image pairs consisting of low resolution and corresponding high resolution images are collected as training data, and the deep neural network is trained to extract pixel-wise features and generate the upsampled super resolution image using the pairs of training data. Dong et al. [1] [2] first used this end-to-end learning-based method with a 2D convolutional neural network (CNN). Though a larger neural network results in improved overall performance [3], training such a deep CNN has been demonstrated to be challenging [4]. Recently, Zhang et al. [6] proposed network with channel attention and residual in residual structure with further enhanced performance in super resolution.

Single image super resolution (SISR) has been adopted into medical image sectors following the rapid advancement in natural images [7] [8] [9]. The majority of previous studies applied the 2D network structures on medical images slice by slice [8] [10]. However, medical images, like Computed Tomography (CT) and MRI, typically contain information about 3D anatomical structures. Processing each image slice independently may lead to mismatch in the adjacent slices or reconstructed images. As a result, 3D models are desired to solve this problem due to their capacity of extracting 3D structural information. According to recent studies, 3D CNNs outperform 2D CNNs by a wide margin in MRI super resolution [11] [12] [13]. However, because of the extra dimension of 3D networks, the demand for a huge amount of GPU resource, as well as longer inference time prevent 3D neural networks to be deployed easily in the real clinics. Although Chen et al. [11] [12] have demonstrated fast 3D models, the margin between the GPU consumption of 2D and 3D networks is still huge.

Regarding to the downsampling methods for synthetic LR image generation, there are two commonly-used approaches. The first one is image-based method using Gaussian blurring [13] [14], which is transferred from generic computer vision tasks without considering the scheme of MR image acquisition. Such gap leads to the inconsistencies between training with synthetic data and inference with real MR images when using the deep learning-based restoration, thus degrade the performance in the real clinics. The second one is the k-space truncation, which is recently recognized as the way of mimicking real LR image acquisition in MRI [16]. Besides, multiple downsampling strategies have been employed in previous research. In the studies of 2D networks,  $2 \times 2 \times 1$  (frequency-encoding (FE)  $\times$  phase-encoding (PE)  $\times$  slice-encoding (SL)) and  $4 \times 4 \times 1$ , as  $\times 2$  and  $\times 4$  in-plane downsampling, were commonly used [14] [16]. And for 3D networks, HR images were downsampled with scale factors of  $1 \times 1 \times 2$ ,  $1 \times 2 \times 2$  or  $2 \times 2 \times 2$  [17] [18] [11] [19]. These downsampling strategies lead to various acceleration factors in acquisition time and different difficulties for SR reconstruction. Therefore, for downsampling strategies with the same acceleration factor, a properly selected downsampling strategy with lower difficulty in SR reconstruction can result in improved performance and more accurate diagnosis. However, the downsampling strategies were not analyzed in previous studies.

Furthermore, patient movement is inevitable during MRI measurements, resulting in motion artifacts that degrades the image quality. Deep learning algorithms can also reduce the motion artifacts and restore the high-quality images [20] [21]. Most of the previous studies utilized 2D UNet-based model to reduce the motion artifacts [22] [23], whereas 3D models may improve the performance of motion artifact reduction while facing the same GPU consumption issue. Besides, previous studies normally used random movement to retrospectively generate motion artifacts [24] [25] [26], making the severity of the motion artifacts uncontrollable and irreproducible.

At last, doctors are frequently concerned about the accuracy of restored high-quality images. Tanno et al. [27] and Qin et al. [28] employed a method to predict aleatoric uncertainty for reconstructed image [30] as auxiliary information to assist doctors. However, such a method can not distinguish whether the uncertainty is caused by the noise in the training data or caused by the error from the deep neural network due to out of distribution (OOD) data, i.e., distribution of training data is not identical to the distribution of test data which is commonly seen in the real clinical environment. The latter is the actual uncertainty which reflects the quality of the restored MR image. On the other hand, the ground-truth (GT) images are available during the training and evaluation of the deep neural network, and the performances of the algorithms are evaluated by calculating the difference or similarity between the output images and the GT using some specific metrics. However, when we apply the deep-learning techniques in clinical settings, GT is no longer available, this Scenario necessitates the use of quantitative methods to estimate the accuracy of restored MR image at both pixel level and overall level to assist the medical doctors to make a trustworthy

diagnostics.

Therefore, with considering the applications of deep learning based MR image restoration, we propose the following methods as contributions in this manuscript:

- 1). Super resolution reconstruction and motion artifact reduction for MR images are similar tasks, which restore the images with corrupted k-spaces. Therefore, we propose a universal convolutional neural network modified from the 2D residual channel attention network [6] with multiple slices input, for multi-tasks in high quality MR image restoration including 3D MRI super resolution and motion artifact reduction. Our model achieved state-of-the-art performance with minimized demands on computation resource and inference time.
- 2). K-space truncation is widely acknowledged as the most realistic low resolution MR image generation method for replacing traditional downsampling methods in computer vision tasks. As a result, the trained model can be applied on in-vivo low resolution images in the real clinic application. Besides, we involved a variety of downsampling strategies, including in-plane down-sampling, through-plane down-sampling and their combination with different scale factors. These downsampling strategies were grouped based on the acquisition time reduction ratio. The super resolution reconstruction performance were evaluated and compared in each downsampling strategy group. The results illustrate the difficulties of super resolution reconstruction with different downsampling strategies, and provide guideline for selecting appropriate low resolution image acquisition strategies.
- 3). Furthermore, we propose a method for retrospectively generating reproducible and quantifiable motion artifacts. With our method, motion artifacts were generated by mimicking the real motion artifact with a predefined motion pattern and controllable severity.
- 4). At last, we developed a method for estimating the pixel-wise uncertainty quantification of generated super resolution MR images. The estimated pixel-wise uncertainty was acquired concurrently with the restored images using the same deep neural network guided by an additional loss component in our method. The correlation between the uncertainty and SSIM / PSNR was further investigated and quantified in our study, providing more trustworthy advice in the diagnosis even when the ground truths are not available.

## II. METHODS AND EXPERIMENTS

In an end-to-end training procedure, our model was designed as a universal network for MR image restoration to learn an accurate inverse mapping of the input low-quality images (LR images or MA corrupted images) to the output high-quality reference images (HR images or original images without MA) and the uncertainty map. During the training phase, the high-quality images were solely used as the system's target. A loss function was computed from the reconstructed and reference images and back-propagated through the layers to

update the network's weights. During the testing phase, the model was fed only low-quality images in order to reconstruct high-quality images and generate uncertainty maps. In the following section, we will go through our proposed network and training procedure in further detail.

Furthermore, the image resolution is determined by the k-space matrix size for a predefined field of view (FOV). Because the acquisition time for 3D imaging is proportional to the phase-encoding steps in the phase-encoding (PE) and slice-encoding (SL) directions, down-sampling of the k-space, which results in lower spatial resolution, is commonly used to accelerate image acquisition. Meanwhile, the resolution in the frequency-encoding (FE) direction is normally bonded to the resolution in the PE direction, implying that the resolution changes simultaneously in the FE and PE directions, whereas the resolution in the SL direction is independent and more flexible. Therefore, down-sampling in SL direction is an alternative to in-plane downsampling which was studied in previous publications for 2D SISR. In our study, we investigated multiple downsampling strategies, including in-plane downsampling, through-plane downsampling and their combinations. They were classified according to acceleration factor. More details are presented in the following section.

Furthermore, we employed the image-based motion artifact generation method with reproducible and quantifiable severity of motion artifact. We designed a pattern of patient movement including in-plane and through-plane movement. The severity of motion artifact can be controlled by adjusting the severity, duration and frequency of movement.

At last, we utilized evidential regression learning to predict the degree of uncertainty in the reconstructed images. Our model generated the uncertainty map concurrently with the reconstructed images guided by the normal-inverse-gamma loss. The generated uncertainty map can be used to predict the accuracy of the reconstructed images when there is no ground truth in the real clinical settings.

#### A. Super-resolution and Motion Artifact Reduction Background

The high-quality image restoration task entails creating a restoration system function,  $h$ , which takes low quality (LQ) images (e.g. low-resolution image, or image with motion artifacts, etc.) and outputs the corresponding reconstructed images (e.g. SR or motion artifact-free images) in high quality (HQ) as shown in the equation below:

$$HQ = h(LQ) \quad (1)$$

For super-resolution task, the LQ image is generated from HR image through resolution degradation function,  $f$ , which usually represents a particular downsampling or performing degradation function as below:

$$LQ = f(HR) \quad (2)$$

It can be found, in order to restore the SR image as close to HR image as possible, the task of designing  $h$  is actually equivalent to find the inverse of function  $f$ :

$$HQ = h(LQ) = f^{-1}(LQ) \quad (3)$$

Prior studies indicate that such task is an ill-posed inverse problem, with no analytical solution to the inverse of  $f$ . Computer vision research has revealed that CNN-based models have great potential to fit the inverse of  $f$  in the generic computer vision domain. CNN-based models have been trained to extract low-level features, build up representative feature space, and accurately reconstruct images from learned features at the same time. As a result, recent studies show that CNN-based approaches achieve state-of-the-art performance in high-quality MR image restoration, including MRI super-resolution and motion-artifact reduction.

Several 2D CNN-based networks were implemented in previous studies to process images with a single slice in each patch [8] [10]. However, the majority of the medical images carry anatomical information in 3D volume. Therefore, 3D CNN-based networks for the restoration of 3D medical images were proposed. Previous research has shown that 3D models outperform 2D models by a wide margin in restoring 3D MR images [11] [12] [13], as cross-slice information can be of tremendous assistance. On the other hand, The additional dimension of a 3D network places a significant strain on computation resources. The number of parameters skyrockets to many times that of 2D networks; the size of image patch grows because 3D patches consist of several slices, resulting in higher VRAM consumption; and the number of operations multiplies due to the extra strides on the third dimension. Due to these factors, we propose a method for processing thin-slab 3D image volume using a 2D CNN-based network.

#### B. Proposed High Quality MR image Restoration Network

Based on the 2D Residual Channel Attention Network (RCAN) [6], which has been proposed in the field of generic computer vision to generate the SR image from the LR image, our network of thin-slab RCAN (TS-RCAN) was developed for 3D MR image restoration. Fig.1 depicts the basic pipeline of our model for high-quality MRI reconstruction. A dedicated module called channel attention (CA) layer is embedded into every residual block in the majority of our model to form a residual channel attention block (RCAB) [5]. A residual group (RG) is formed by several RCABs and a long skip connection, and the same pattern has also been extended to form a residual in residual (RIR) module, which also includes several RGs and a long skip connection. The attention weights for different channels that carry the statistics of semantic information of the MR image feature maps will be learned and used to guide the network focusing on restoration of the more important semantic information. Meanwhile, the skip connection in RCAB, RG, and RIR could provide the possibility of training the network model at a quick pace, especially if the network focuses on learning high frequency information by directly bypassing low frequency information. Back propagation is used to adjust all of the network's weights, which is driven by the minimization of the primary and refinement loss functions, which represent differences between predicted HQ MR images and ground truth images. When the LR images in the super resolution task are downscaled, the

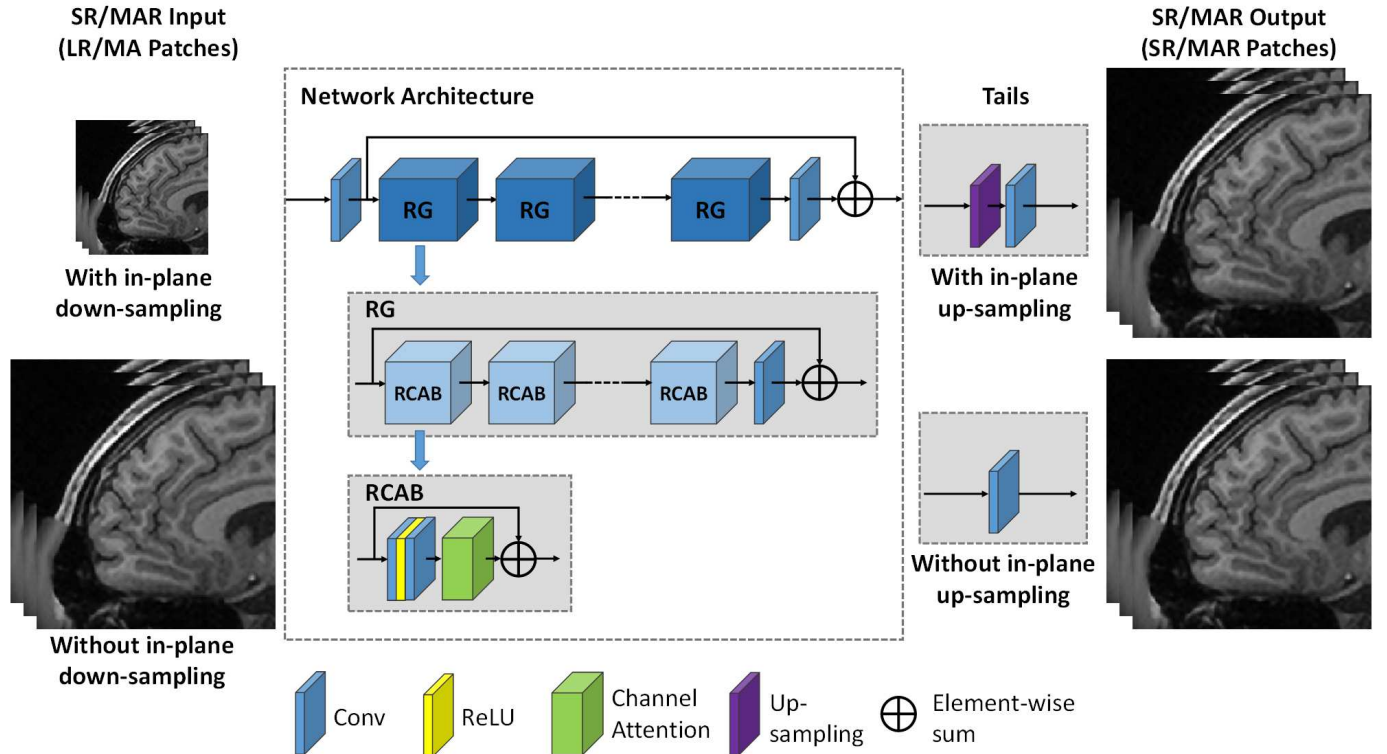


Fig. 1: The pipeline of TS-RCAN based MRI SR and MAR network

upsampling module performs the upscaling operation on the learned feature maps, resulting in the same size of the SR and HR images.

In the MRI SR task, the HR images had a larger matrix size compared to the generated LR images along the down-sampled directions. We constructed the TS-RCAN model with  $N$  RGs,  $M$  RCABs per RG, and an up-sampling module if an in-plane upscaling image is needed. The 2D LR images with a single channel or the 3D LR images with the third dimension placed on the channels were processed to generate corresponding 2D/3D SR images. In the motion artifact reduction task, the MA corrupted images have the same size as the MA reduced (MAR) images, so the upsampling module was removed.

In our experiment, we used the TS-RCAN to process both single-slice (in 2D mode) and thin-slab (in 3D mode) MR image patches. The 2D network is intrinsically capable of processing 3D datasets because of its channel dimension. Therefore, the network was applied in a multi-channel input and multi-channel output mode, with the third dimension of the 3D image patch placed on the channel dimension. We assume the first convolutional layer of the network has the number of input channels as  $M$  ( $M \leq 5$ ) and the number of output channels as  $N$ , and the size of the input image patches  $M \times H \times W$ . Therefore, the convolution kernel size of the first layer is  $N \times M \times H \times W$ , which works equally to the convolution with a 3D convolution kernel, whose size is  $N \times 1 \times M \times H \times W$  with non-padding. In this step, features of multiple input slices were extracted and compressed into a single channel feature map for  $N$  times with different filters. Afterwards, these extracted features are learnt

to reconstruct the high quality images in the hidden layers. At the last convolutional layer of the network, the number of the output channels equals the expected slice number of the target patch. The only difference between our 2D network and conventional 3D networks in this scenario is the smaller number of slices in each patch, which prevents through-plane features from being extracted over a larger slice range. Our experiments revealed that the features extracted from a thin-slab volume were sufficient for reconstructing high quality multi-slice images, and our model outperformed 3D networks and demand minimal computation resources.

In addition, in order to improve the performance even more, we used a different type of self-ensemble in our experiments. Network-based and data-based ensemble methods are commonly proposed to improve the performance of neural networks. A network-based ensemble uses several de-correlated trained networks or repeats the inference with different dropouts, whereas a data-based ensemble uses data augmentation, in which original images are rotated, flipped, or re-scaled before being fed to the network, and then transformed back to their original position and scale after inference. All of these traditional ensemble methods, on the other hand, require more time in terms of training or operation complexity. To make use of the ensemble, we used a simple but effective strategy. In the 3D mode of our network, each patch consisted of several slices, each of which appeared in different places in different patches and was processed by the network differently, resulting in multiple outputs for the same image slice. Our experiments revealed that the average of all the outputs for the same slice achieved higher values in all metrics than every

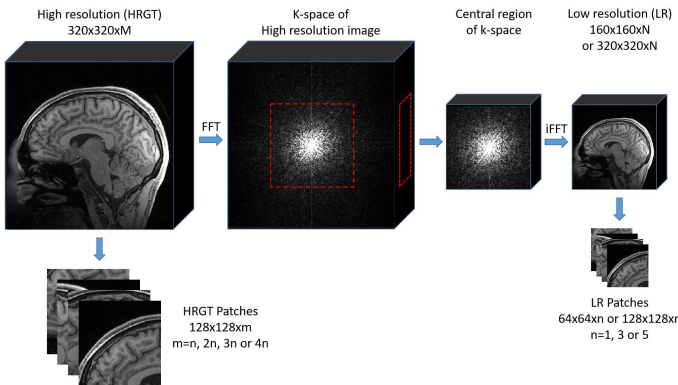


**Fig. 2:** Generation of 3D LR MR images with scale factor of 2 in three directions and patch cropping

output image of this slice. Our method doesn't require any additional operations or training time.

### C. Down-sampling Strategies for Super-resolution

A k-space truncation was used, as opposed to super-resolution tasks for visual images, where the low-resolution images are generated using bicubic or Gaussian blurring down-sampling. In order to acquire MR images, the signal in the frequency domain is collected to form the k-space, which is then transformed to the image domain using inverse Fast Fourier Transformation to reconstruct the image (iFFT). With k-space truncation down-sampling, The images were first transformed into k-space with Fast Fourier Transformation (FFT), then the central region of k-space with varying sizes based on the down-sampling factor was retained, and the surrounding region was truncated. At last, the truncated k-space was transformed back to the image domain with iFFT. The intensities of voxels were scaled to 0 and 1 for both high resolution and generated low-resolution images. Fig.2 shows an example of 3D LR MR image generation.

The acquisition time for 3D MRI is highly dependent on phase-encoding steps in the PE and SL directions, only downsampling in PE and SL directions shortens the acquisition time. However, in regular MRI measurements, a decrease in resolution in the PE direction also leads to a decrease in resolution in the FE direction with the same scale factor to maintain the isotropic in-plane resolution, resulting in unnecessary loss of k-space regions and greater difficulty in restoring the HR image. Meanwhile, the slice thickness is independent from the in-plane resolution and can be downsampled with greater flexibility. More specifically, when a  $\times 2$  acceleration is expected, there are two down-sampling options, which are  $2 \times 2 \times 1$  and  $1 \times 1 \times 2$ . With the  $2 \times 2 \times 1$  down-sampling, 75% of the k-space is lost, while with  $1 \times 1 \times 2$  only 50% of the k-space is lost.

However, the difficulty of restoring HR image is not solely determined by the ratio of truncated k-space. The more low-frequency components of the k-space are dropped, the more difficult it is to restore the HR image. In this study, we investigated multiple downsampling strategies and their super resolution reconstruction performances. Based on the regular

MRI measurement process, we tested the super resolution reconstruction with the down sampling factors of  $2 \times 2 \times 1$  and  $1 \times 1 \times 2$  for  $\times 2$  acceleration, and  $4 \times 4 \times 1$ ,  $2 \times 2 \times 2$ , and  $1 \times 1 \times 4$  for  $\times 4$  acceleration.

After downsampling, the HR and LR images were cropped into patches of smaller sizes to save computation resources. For 2D models, each slice of the HR images was cropped into  $128 \times 128$  patches with 32 voxels overlapped between neighbouring patches to avoid artifacts on the edges of the patches. The LR images were cropped into  $64 \times 64$  patches with 16 voxels overlapped for a scale factor of 2 and  $32 \times 32$  patches with 8 voxels overlapped for a scale factor of 4. Each LR patch contains  $1/3/5$  neighbouring slices from the LR image with  $n - 1$  slices overlapped between neighbouring patches, and the number of slices for the HR patch is  $1/3/5$  times the scale factor in the SL direction. For 3D models, the LR images were interpolated to the same matrix size as the HR images, since 3D models don't have an upsampling module. Both the HR and LR images were cropped into  $64 \times 64 \times 64$  patches with 32 voxels overlapped between neighbouring patches.

### D. Motion Pattern and Motion Artifact Quantification

The method of splicing lines from multiple k-spaces was used to simulate the generation of real motion artifacts in MR images for the retrospective generation of motion artifacts. As shown in Fig.3A, a group of images were generated from the original image volume by rotating it in specific directions and to specific degrees. The original image and generated images were then transformed to k-space using FFT, and k-space segments of the original image were replaced with segments from the generated images' k-spaces, according to a predefined pattern. The images for the motion-artifact correction task were not cropped, so the axial sizes of the input MA and GT images were  $320 \times 256$ .

Regarding the motion patterns, we employed simplified and commonly-recognized patterns of motion in brain imaging, which were head rotation as the in-plane movement and nodding as the through-plane movement, and the severity was managed by the frequency of motion. The scheme of the motion pattern is depicted in Fig.3B. We used echo-group (EG) as a unit of the minimal time period in which a certain number of successive echos were acquired (which can also be considered as the TR for sequences from the turbo-spin-echo family), and the duration of any action must be an integer multiple of EG. In terms of the type of movement, we used head rotations of 5 degrees to the left and to the right, with and without head nodding by 5 degrees. Therefore, the whole process of patient movement was set as below:

- 1) : at  $t = 0$ , the patient stayed in the original position and stayed for  $T_S$ ;
- 2) : from  $t = T_S$  to  $t = T_S + 2EG$ , the patient's head rotated to the left for 5 degrees;
- 3) : from  $t = T_S + 2EG$  to  $t = T_S + 7EG$ , the patient's head stayed at the position of 5 degrees to the left;
- 4) : from  $t = T_S + 7EG$  to  $t = T_S + 9EG$ , the patient's head rotated back to the starting position;

5) : from  $t = T_S + 9EG$  to  $t = 2T_S + 9EG$ , the patient's head stayed in the starting position;  
 6) : from  $t = 2T_S + 9EG$  to  $t = 2T_S + 18EG$ , the patient's head rotated to the right and returned to the starting position following the same process of step 2 to 4;  
 7) : from  $t = 2T_S + 18EG$  to  $t = 3T_S + 18EG$ , the patient's head stayed in the starting position.

The process from steps 2 to 7 was repeated until the whole k-space was acquired, and head nodding was performed together with head rotating. The severity of motion artifacts was controlled by  $T_s$  and EG.

In our study,  $T_s$  was set to 9EG, 18EG, 36EG and 72EG, leading to a corrupted k-space line ratio of 50%, 33.3%, 20% and 11.1%. 1EG consists of 80 echos. A centric trajectory was selected to fill the k-space. The SSIMs and PSNRs of the images with different severities of motion artifacts follow a linear tendency as shown in Table III in the result section.

### E. Uncertainty

In previous studies, the pixel-wise aleatoric uncertainty can be generated by incorporating Gaussian negative log likelihood (NLL) loss into neural network [29], and applied in MR super-resolution reconstruction [27] [28]. Such uncertainty only represents the uncertainty from data, which cannot be prevented, and it is not the main issue when applying the deep learning based MRI restoration in clinical practices. On the contrary, the inevitable OOD data issue (i.e., images acquired from different patients or from a different scanner may have diverse distributions in a real clinic environment due to image quality differences) can be represented by epistemic uncertainty [30]. In our study, both pixel-wise aleatoric uncertainty and epistemic uncertainty are estimated by using evidential regression [31]. Evidential deep learning formulates learning as an evidence acquisition process. Every training example adds support to a learned higher-order, evidential distribution. Sampling from this distribution yields instances of lower-order likelihood functions from which the data was drawn. Instead of placing priors on network weights, as is done in Bayesian neural networks, evidential approaches place priors directly over the likelihood function. By training a neural network to output the hyperparameters of the higher-order evidential distribution, a grounded representation of both epistemic and aleatoric uncertainty can then be learned without the need for sampling. Amini et al. proposed the method to estimate a posterior distribution  $q(\mu, \sigma^2)$ , and the approximation to the posterior distribution takes the form of the Gaussian conjugate prior, the Normal Inverse-Gamma (NIG) distribution  $p(\mu, \sigma^2 | \gamma, v, \alpha, \beta)$  [31]. Afterwards, the prediction and uncertainties can be calculated as:

$$\text{Prediction} : E[\mu] = \gamma \quad (4)$$

$$\text{Aleatoric} : E[\sigma^2] = \frac{\beta}{\alpha - 1} \quad (5)$$

$$\text{Epistemic} : \text{Var}[\mu] = \frac{\beta}{v(\alpha - 1)} \quad (6)$$

Furthermore, we investigated the relationships between epistemic uncertainty and the SSIM and PSNR metrics of

the reconstructed images. Linear regression and exponential regression were performed to estimate the correlation of epistemic uncertainty to SSIM and PSNR for the test datasets, respectively. Then, the obtained regression curves can be used to estimate the SSIM and PSNR of the reconstructed images when ground truth is not available.

### F. Loss Functions

In previous studies, different types of loss functions were used to train neural networks for specific feature refinements. In this study, pixel-wise Charbonnier loss [32] was used as a differentiable L1 loss to avoid a strong smoothing effect [33]:

$$L_{Char} = \frac{1}{N} \sum_{i=1}^N \sqrt{(HR_i - SR_i)^2 + \epsilon} \quad (7)$$

where  $\epsilon$  is assigned as  $10^{-4}$ .

Furthermore, in some of the most recent studies, SSIM loss is used to drive the network reconstructing the high quality images toward better structural similarity with the GT images. It is typically applied as 1 subtracted by the SSIM value measured between the reconstructed images and the GT images [34] [35]. In this study, we utilized the L1 loss of the square of the SSIM value to enhance the weight of SSIM loss:

$$L_{SSIM} = \frac{1}{N} \sum_{i=1}^N |1 - SSIM(SR_i, HR_i)^2| \quad (8)$$

The calculation of SSIM will be introduced in latter section.

In our study, we utilized the weighted sum of Charbonnier loss and SSIM loss for image restoration:

$$\text{Loss} = L_{Char} + \alpha_1 L_{SSIM} \quad (9)$$

where  $\alpha_1 = 0.5$  in our study for the best performance.

Besides, the Normal-inverse-Gamma loss [31] was employed when the uncertainty map was demanded:

$$L_{NIG} = L_{NLL} + \lambda L_{Reg} \quad (10)$$

where

$$\begin{aligned} L_{NLL} = & \frac{1}{2} \log\left(\frac{\pi}{v}\right) - \alpha \log(\Omega) \\ & + \left(\alpha + \frac{1}{2}\right) \log((y - \gamma)^2 v + \Omega) \\ & + \log\left(\frac{\Gamma(\alpha)}{\Gamma(\alpha + \frac{1}{2})}\right) \end{aligned} \quad (11)$$

$$\Omega = 2\beta(1 + v) \quad (12)$$

$$L_{Reg} = |y - \gamma| (2v + \alpha) \quad (13)$$

$\alpha, \beta, \gamma$  and  $v$  are the outputs of the network.  $y$  is the ground truth.

To summarize, we utilized the weighted sum of Charbonnier loss and SSIM loss for image restoration, and NIG loss when evidential regression was employed:

$$\text{Loss} = L_{Char} + \alpha_1 L_{SSIM} + \alpha_2 L_{NIG} \quad (14)$$

where 0.5 and 1 were selected as the value of  $\alpha_1$  and  $\alpha_2$  in our study for the best performance.

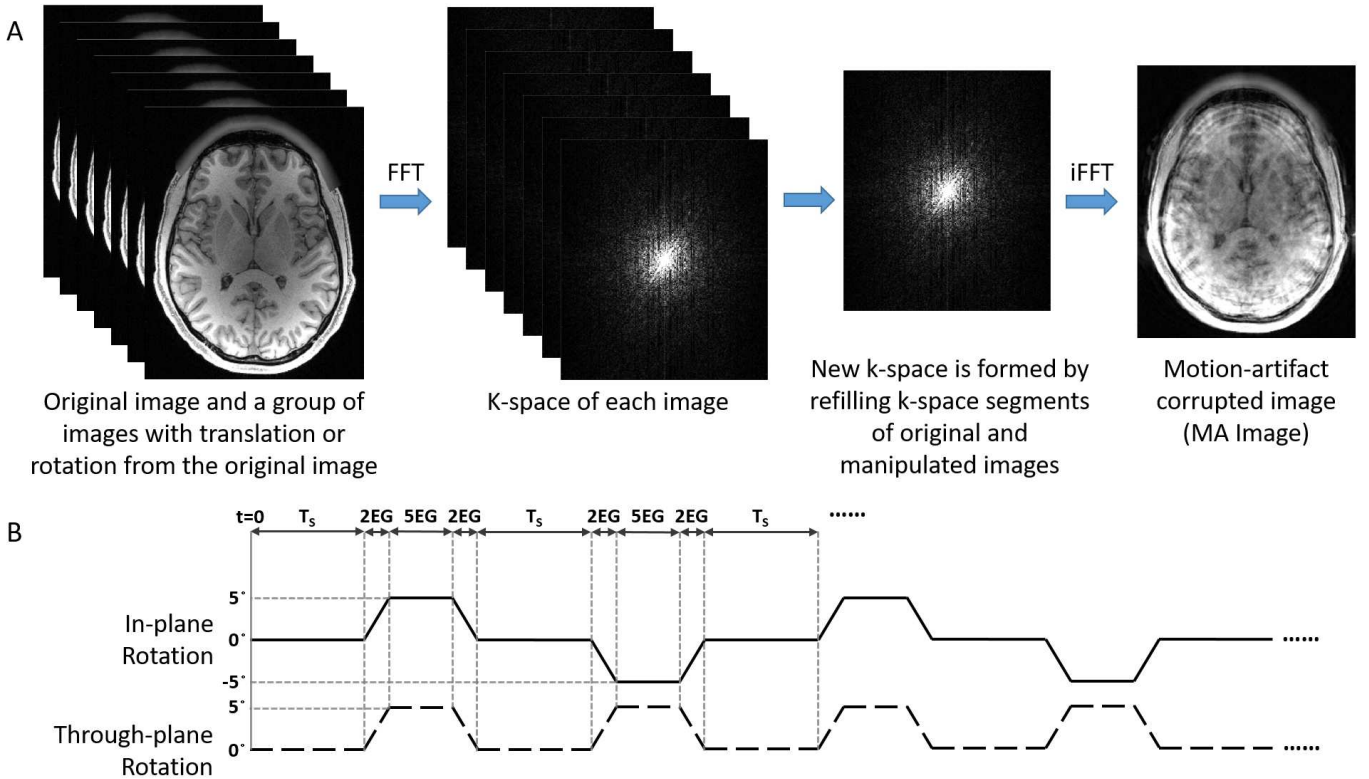


**Fig. 3:** A: Image-based generation of motion-artifact in MR images; B: Scheme of motion pattern employed in our study.

### G. Datasets

In this study, we used the T1w images from the Human Connectome Project (HCP) dataset [36], consisting of multi-contrast images from 1113 patients. The T1w images were acquired in the sagittal direction with 3D MPRAGE on the Siemens 3T PRISMA platform. The matrix size was 320x320x256, with an isotropic resolution of 0.7 mm. In our experiments, we randomly selected 80/10/10 patients from the HCP patient cohort for training/validation/test groups. The training datasets were used to train the neural networks, the validation datasets to monitor the neural networks' performance during training, and the test datasets to evaluate the neural networks after training. There were no shared datasets among the three groups. In addition, to verify the quantified correlation between uncertainty and SSIM/PSNR, we used another 40 datasets which were isolated from the previously mentioned training/validation/test groups.

### H. Implementation Details

In terms of TS-RCAN implementation, for an SR factor of 2, an RG number of 5 was chosen, with 5 RCABs in each RG. The convolution layers in shallow feature extraction and the RIR structure had 64 filters, except that for channel downscaling. We connected two stages of the TS-RCAN network sequentially for progressive-upsampling with an SR factor of 4. Each stage consisted of 3 RGs with 3 RCABs and one upsampling module upscaling the LR images by a factor of 2 at the end of each stage.

The networks were trained on a workstation equipped with two Quadro GV100 graphic cards (Nvidia, Santa Clara, Calif). For all deep learning experiments, we used Pytorch 1.7 as the back end. In each training batch, eight LR patches were randomly extracted as inputs. We trained our model for 50 epochs using the ADAM optimizer with  $\beta_1 = 0.9$ ,  $\beta_2 = 0.999$ , and  $\epsilon = 10^{-8}$ , and a Cosine-decay learning rate was applied starting from  $10^{-4}$  and ending at  $10^{-8}$ .

We employed peak signal-to-noise ratio (PSNR) and structure similarity index (SSIM) [34] to evaluate the quality of reconstructed images:

$$PSNR(x, y) = 10 \log_{10} \left( \frac{\max(y)^2}{MSE(x, y)} \right) \quad (15)$$

$$MSE(x, y) = \frac{1}{N} \sum_{i=1}^N (x_i - y_i)^2 \quad (16)$$

$$SSIM(x, y) = \frac{(2\mu_x\mu_y + C_1)(2\sigma_{xy} + C_2)}{(\mu_x^2 + \mu_y^2 + C_1)(\sigma_x^2 + \sigma_y^2 + C_2)} \quad (17)$$

where  $\mu_x$  and  $\mu_y$  are the means of x and y representing the luminance of the images,  $\sigma_x^2$  and  $\sigma_y^2$  are the variances of x and y representing the contrast of the images, and  $\sigma_{xy}$  is the covariance of x and y measuring the tendency of x and y to vary together.  $C_1$  and  $C_2$  are small constants.

## III. RESULTS AND DISCUSSION

**TABLE I:** Comparison of SR performance with different down-sampling strategies (red represents the best and blue represents the second best)

Scale Factor	Acceleration Factor	# Input / Output Slices	# Params (M)	# Ops (GFlop)	Inference Time (s)	SSIM / PSNR
$2 \times 2 \times 1$	$\times 2$	1 / 1	2.23	9.09	5.97	0.9625 / 38.7468
		3 / 3	2.23	9.12	5.93	<b>0.9631 / 38.8662</b>
		3 / 3 +	2.23	5.93	5.93	<b>0.9634 / 38.9355</b>
		5 / 5	2.24	9.14	5.86	0.9627 / 38.7745
		5 / 5 +	2.24	9.14	5.86	0.9631 / 38.8605
$1 \times 1 \times 2$	$\times 2$	1 / 2	2.08	33.95	7.09	0.9558 / 38.5996
		3 / 6	2.09	33.99	7.16	0.9724 / 40.7656
		3 / 6 +	2.09	33.99	7.16	0.9725 / 40.8979
		5 / 10	2.09	34.05	6.87	<b>0.9736 / 40.9537</b>
		5 / 10 +	2.09	34.05	6.87	<b>0.9739 / 41.1143</b>
$4 \times 4 \times 1$	$\times 4$	1 / 1	2.88	7.36	7.32	0.9272 / 35.5164
		3 / 3	2.88	7.38	7.17	0.9291 / 35.6303
		3 / 3 +	2.88	7.38	7.17	<b>0.9300 / 35.7243</b>
		5 / 5	2.88	7.40	7.54	0.9289 / 35.4683
		5 / 5 +	2.88	7.40	7.54	<b>0.9301 / 35.5939</b>
$1 \times 1 \times 4$	$\times 4$	1 / 4	2.09	33.96	3.58	0.9148 / 34.1939
		3 / 12	2.09	34.05	3.57	0.9450 / 36.9546
		3 / 12 +	2.09	34.05	3.57	0.9449 / 37.0753
		5 / 20	2.10	34.15	3.38	<b>0.9458 / 37.0159</b>
		5 / 20 +	2.10	34.15	3.38	<b>0.9463 / 37.2224</b>
$2 \times 2 \times 2$	$\times 4$	1 / 2	2.23	9.10	3.02	0.9356 / 36.0732
		3 / 6	2.24	9.15	2.98	0.9490 / 37.5758
		3 / 6 +	2.24	9.15	2.98	<b>0.9494 / 37.6909</b>
		5 / 10	2.24	9.19	2.97	0.9491 / 37.5689
		5 / 10 +	2.24	9.19	2.97	<b>0.9498 / 37.7166</b>

### A. Super-Resolution with Different Down-sampling Strategies

In this section, we will first assess our network’s performance in 2D and 3D mode for SR image reconstruction from LR images generated by various down-sampling strategies, and then compare the difficulty of SR image reconstruction among these down-sampling strategies.

Table I shows the performance of SR reconstruction using our network in both 2D and 3D modes. For all downsampling strategies, 3D mode clearly outperformed 2D mode. The SSIM and PSNR values of SR images reconstructed with 3-slice input increased significantly from single-slice input and rose again with 5-slice input for the strategies with through-plane downsampling. The SSIM and PSNR values for the strategies with only in-plane downsampling reached their peaks at 3-slice input and dropped slightly with 5-slice input. In addition, self-ensemble improved the performance of the 3D mode in the SR reconstruction from all downsampling strategies. Furthermore, with our network, there was only a minor increase in the number of parameters and the number of operations within each downsampling strategy when the network switched from 2D to 3D mode.

Furthermore, the SR reconstruction performance is compared between different downsampling strategies with the same acceleration factors in Table I. With an acceleration factor of 2, the SSIM and PSNR values of  $1 \times 1 \times 2$  downsampling are more than 0.01 and 2.2 dB higher than those of  $2 \times 2 \times 1$ , respectively. And with the acceleration factor of 4, the  $2 \times 2 \times 2$  downsampling has the highest values of SSIM and PSNR, which are 0.003 and 0.5 dB higher than  $1 \times 1 \times 4$  and 0.02 and 2.1 dB higher than  $4 \times 4 \times 1$ . The results reveal that it is easier to reconstruct accurate SR images from  $1 \times 1 \times 2$  downsampling for  $\times 2$  acceleration and  $2 \times 2 \times 2$

for  $\times 4$  acceleration.

In addition to the difference in the metrics, the visual effect is compared in Fig.4. The difference between 2D and 3D SR is revealed in Fig.4A. The 2D SR image shows errors in reconstructing small anatomical structures in the sagittal view, whereas the 3D SR image shows extensive accuracy in restoring small anatomical structures. Furthermore, in the axial view of the 2D SR image, but not in the 3D SR image, there is a mismatch of neighboring slices. Fig.4B compares SR images from various downsampling strategies with an acceleration factor of 4, highlighting the limitations of the  $4 \times 4 \times 1$  and  $1 \times 1 \times 4$  downsamplings for SR reconstruction. The reconstructed image of  $4 \times 4 \times 1$  loses nearly all the small anatomical structures in the sagittal view and  $4 \times 4 \times 1$  in the axial view, while the image reconstructed from  $2 \times 2 \times 2$  is less blurry than the previous two with the majority of the small anatomical structures retained.

### B. Super-Resolution Compared with the State of the Art

As mentioned in previous studies, 3D CNNs outperform 2D CNNs by a wide margin in MRI super resolution [11] [12] [13], and our experiments show the same results in Section IIIA. Therefore, we only compare 3D SR in this section. We implemented the previously published state-of-the-art models, including DCSRN [11] and mDCSRN [12], and extended SRCNN [37] and FSRCNN [38] to 3D mode, as the baseline to compare with our model for 3D SR. All the models were trained with the same number of epochs and settings (i.e. learning rate decay and optimizer). With respect to quantitative similarity metrics, as shown in Table II, our model with 3D SR highly outperformed all previous SISR models in 3D SR tasks, consumed less GPU resource and less inference time than most of the previous models.

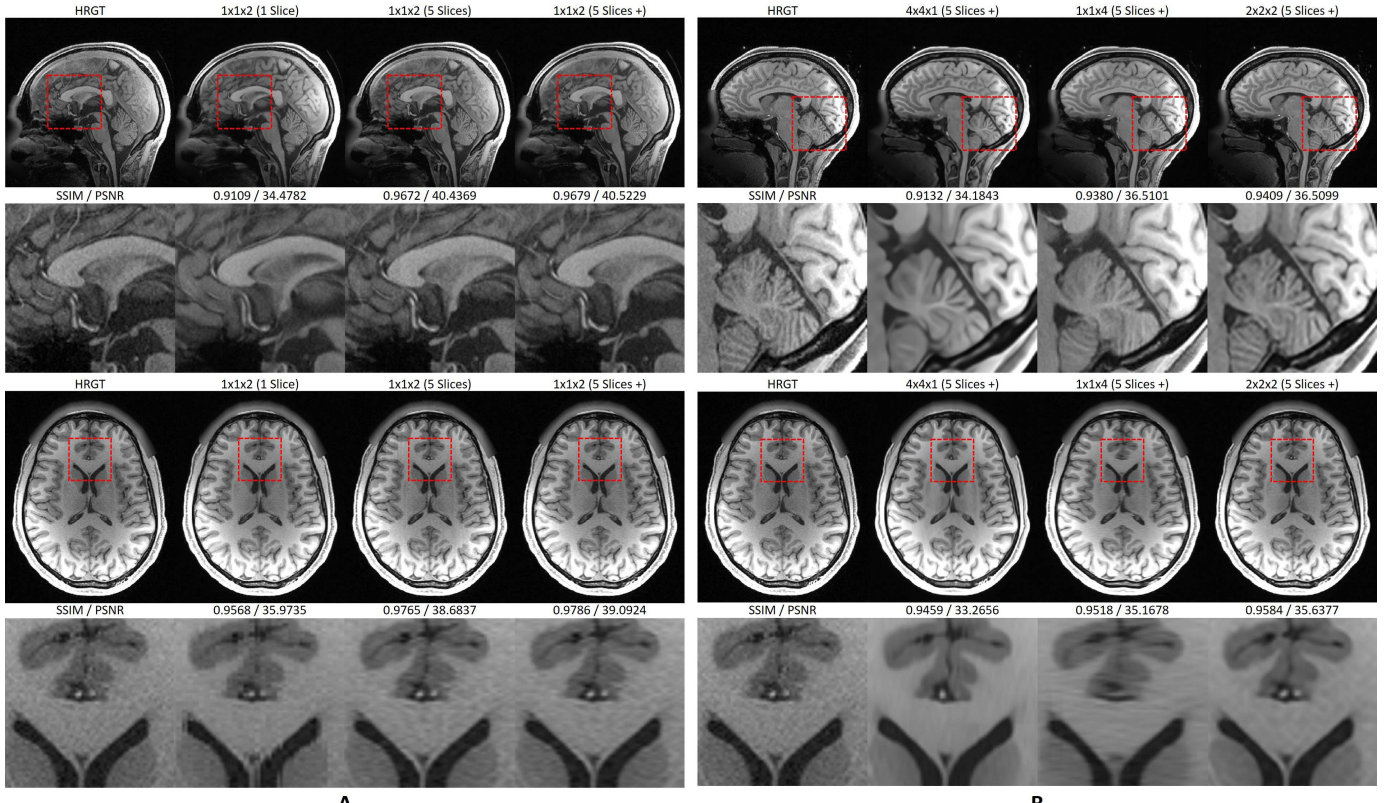


**Fig. 4:** Visual effect comparison of super resolution. Left: SR in single-slice and thin-slab mode; Right: different downsampling strategies with acceleration factor of 4.

**TABLE II:** Comparison with the MRI super resolution state-of-the-art methods (red represents the best and blue represents the second best)

Model	Scale Factor	# Ops (GFlops)	GPU Consumption (GB)	Inference Time (s)	SSIM / PSNR
Bicubic	$2 \times 2 \times 1$	N/A	N/A	N/A	0.9227 / 33.6546
3D SRCNN		13.841	2.48	3.00	0.9540 / 36.8319
3D FSRCNN		7.079	3.22	3.68	0.9540 / 36.8748
DCSRN [11]		57.50	9.35	10.84	0.9535 / 36.8042
mDCSRN [12]		107.54	14.13	28.16	0.9591 / 37.5905
TS-RCAN (Ours)		9.12	1.48	5.93	<b>0.9631 / 38.8662</b>
TS-RCAN+ (Ours)		9.12	1.48	5.93	<b>0.9634 / 38.9355</b>
Bicubic	$4 \times 4 \times 1$	N/A	N/A	N/A	0.8117 / 27.3231
3D SRCNN		13.841	2.48	3.02	0.8995 / 33.1843
3D FSRCNN		7.079	3.22	3.68	0.8984 / 33.0282
DCSRN [11]		57.50	9.35	10.83	0.8984 / 33.1024
mDCSRN [12]		107.54	14.13	28.13	0.9159 / 34.1952
TS-RCAN (Ours)		7.396	1.62	7.17	<b>0.9291 / 35.6303</b>
TS-RCAN+ (Ours)		7.396	1.62	7.17	<b>0.9300 / 35.7243</b>
Tricubic	$2 \times 2 \times 2$	N/A	N/A	N/A	0.8964 / 31.5198
3D SRCNN		13.841	2.48	3.03	0.9403 / 35.8376
3D FSRCNN		7.079	3.22	3.71	0.9405 / 35.8810
DCSRN [11]		57.50	9.35	10.79	0.9398 / 35.8276
mDCSRN [12]		107.54	14.13	28.12	0.9469 / 36.3776
TS-RCAN (Ours)		9.19	1.48	2.97	<b>0.9491 / 37.5689</b>
TS-RCAN+ (Ours)		9.19	1.48	2.97	<b>0.9498 / 37.7166</b>

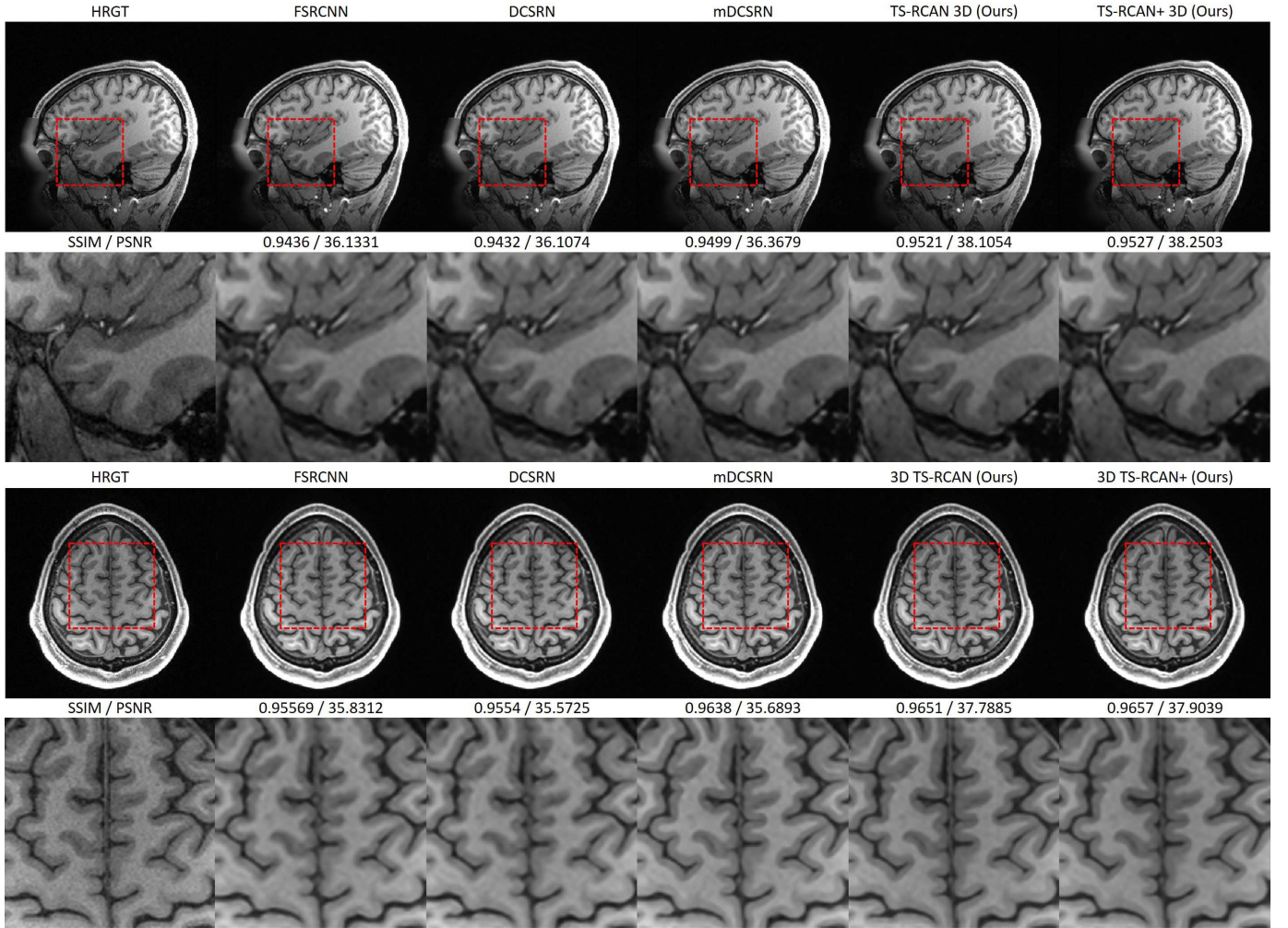


Fig. 5: Visual effect comparison with the MRI super resolution state-of-the methods on  $2 \times 2 \times 2$  SR

For SR reconstruction from  $2 \times 2 \times 1$  downsampling, our model achieved 0.9631 in SSIM and 38.8662 in PSNR, which were 0.004 and 1.3 dB higher than mDCSRN, respectively. Self-ensemble improved the performance of our model even more. Our model outperformed the other models in SSIM and PSNR for SR reconstruction from  $4 \times 4 \times 1$  downsampling by more than 0.013 and 1.4 dB, respectively. For SR reconstruction from  $2 \times 2 \times 2$  downsampling, our model outperformed the mDCSRN by 0.002 and 1.2 dB without self-ensemble, and 0.003 and 1.3 dB with ensemble in SSIM and PSNR, respectively.

In terms of the number of operations, our model ranks second among all models for all scale factors. Furthermore, our model consumes the least VRAM for inference, accounting for 10.4% of mDCSRN's VRAM consumption across all scale factors. In addition, for 3D SR reconstruction, the inference time of our models ranges from 10.6% to 25.5% of mDCSRN.

Fig. 5 depicts the visual difference between the 3D SR of various networks with  $2 \times 2 \times 2$  downsampling. The reconstructed SR images of FSRCNN and DCSRN are still highly blurry in the sagittal view, whereas the others are comparable in sharpness. In the axial view, our network demonstrates improved accuracy in the reconstruction of small anatomical

structures.

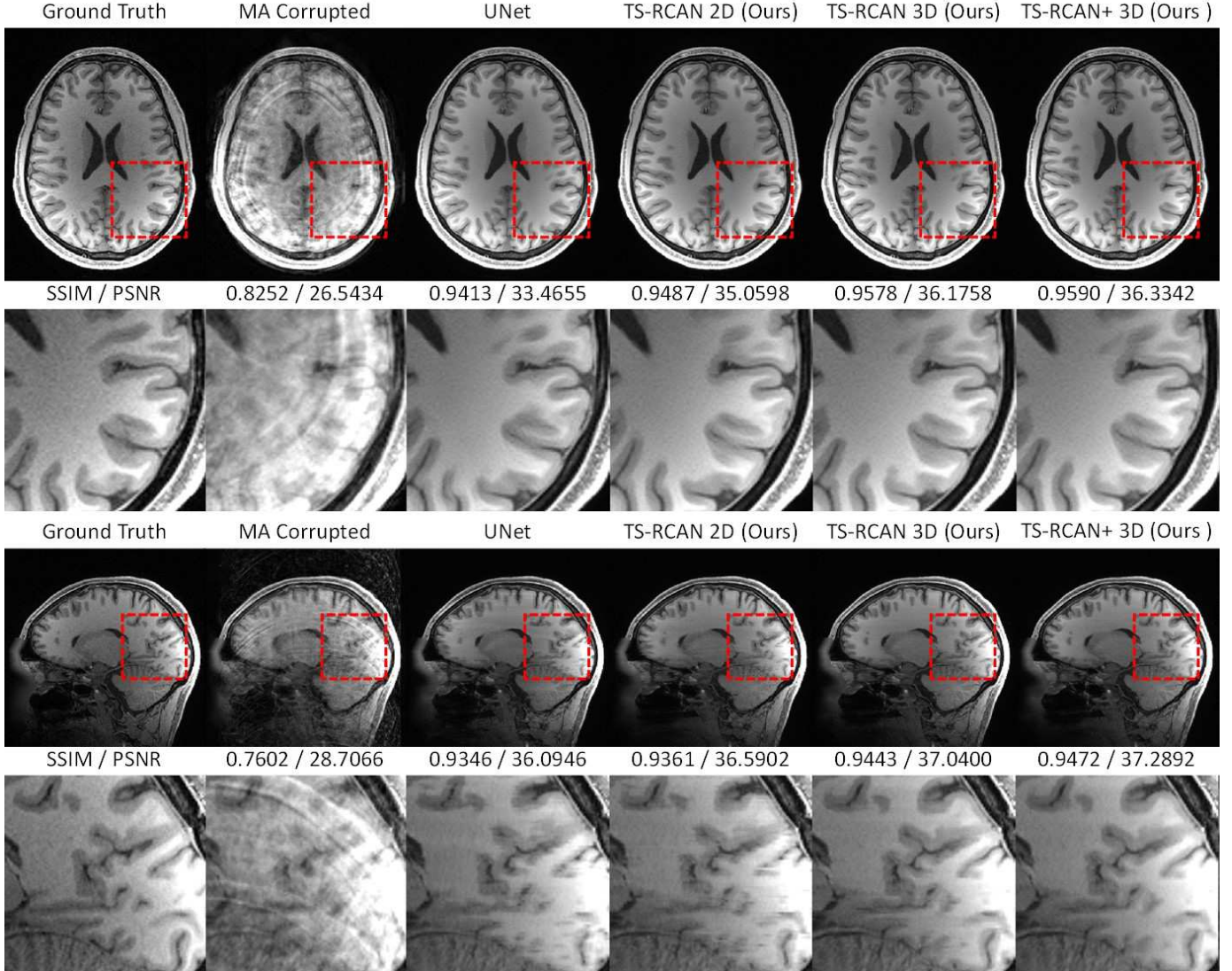
### C. Motion Artifact Generation and Reduction

In previous studies, motion artifacts were typically generated by random movement and corrupting randomly selected k-space lines, resulting in non-reproducible motion artifact severity. Our motion artifact generation method employs pre-defined motion patterns with specific durations and repetitions at specific frequencies, resulting in controllable severity. As shown in Table III, the SSIMs and PSNRs of the motion artifact-corrupted images, which reveal the severity difference of motion artifacts, follow a consistent tendency as the  $T_s$  increases. When the  $T_s$  is doubled in the group with only in-plane rotation, the SSIM increases by 0.049 to 0.074 and the PSNR increases by 2.5 to 3.3 dB. The SSIM and PSNR of the group with both in-plane and through-plane rotation exhibit the same pattern. Furthermore, the comparison between these two groups reveals that through-plane rotation results in additional decrements of 0.003 to 0.012 in SSIM and around 0.4 to 0.5 dB in PSNR.

Also demonstrated in Table III, our network outperformed the UNet [22], which was widely used in previous studies,

**TABLE III:** Motion Artifact Reduction Performance (red represents the best and blue represents the second best)

In-plane / Through-plane Rotation	$T_S$	Before Correction SSIM / PSNR	U-Net [22] SSIM / PSNR	TS-RCAN 2D (Ours) SSIM / PSNR	TS-RCAN 3D (Ours) SSIM / PSNR	TS-RCAN+ 3D (Ours) SSIM / PSNR
5 / 0	9EG	0.7515 / 28.4205	0.9334 / 36.1477	0.9378 / 36.6720	<b>0.9434 / 37.0669</b>	<b>0.9447 / 37.1948</b>
5 / 0	18EG	0.8142 / 30.9466	0.9547 / 37.8081	0.9573 / 38.4131	<b>0.9608 / 38.7964</b>	<b>0.9615 / 38.8977</b>
5 / 0	36EG	0.8843 / 34.6632	0.9726 / 40.2495	0.9742 / 41.0761	<b>0.9762 / 41.3078</b>	<b>0.9766 / 41.3979</b>
5 / 0	72EG	0.9335 / 37.9792	0.9815 / 42.4534	0.9824 / 43.0007	<b>0.9838 / 43.3416</b>	<b>0.9841 / 43.4338</b>
5 / 5	9EG	0.7391 / 27.8964	0.9319 / 35.5853	0.9349 / 36.0326	<b>0.9428 / 36.6468</b>	<b>0.9442 / 36.7868</b>
5 / 5	18EG	0.8051 / 30.4936	0.9538 / 37.3098	0.9564 / 37.9584	<b>0.9601 / 38.3078</b>	<b>0.9609 / 38.4133</b>
5 / 5	36EG	0.8798 / 34.2659	0.9726 / 40.0343	0.9742 / 40.6765	<b>0.9760 / 41.0267</b>	<b>0.9764 / 41.1266</b>
5 / 5	72EG	0.9301 / 37.5567	0.9804 / 41.5370	0.9815 / 42.1384	<b>0.9830 / 42.4736</b>	<b>0.9834 / 42.5703</b>

**Fig. 6:** Comparison of visual effect on axial and sagittal planes among methods for MAR with  $T_S = 9EG$  and the combination of 5 degrees in-plane and through-plane rotation.

with considerable gains in SSIM and PSNR. In 2D mode (1 slice input and output), our network highly outperformed the UNet with consistent improvements of 0.001 to 0.003 SSIM and 0.5 to 0.7 dB in PSNR for varying degrees of motion artifact severity. The performance of our network was further improved in 3D mode, with increments of 0.001 to 0.008 in SSIM and 0.3 to 0.6 dB in PSNR compared to 2D mode. Furthermore, the self-ensemble raised the SSIM and PSNR

by another 0.001 and 0.1 dB, respectively.

The visual effects of motion artifact reduction are also compared, and our network shows significant improvement. Fig.6 depicts an example of images in the axial and sagittal planes with motion artifacts reduced from the worst case. On the axial plane, the UNet corrected image contains several incorrectly restored anatomical structures when compared to the ground truth, whereas with our network in 2D mode, the

quality of the restored image is improved with minor anatomical structure errors. And in 3D mode, our model provides significantly improved image quality, with the majority of features retained and very well represented. The difference between the models is even greater in the sagittal plane. Due to a lack of through-slice information, the UNet generated image contains a severe through-slice mismatch, which is slightly reduced by our model in 2D mode and significantly reduced in 3D mode.

#### D. Restoration with Uncertainty

The uncertainty maps were generated simultaneously with the restored images using our network with NIG loss. In this section, the aleatoric and epistemic uncertainty for the super resolution task will be qualitatively and quantitatively evaluated. Firstly, an example of an HRGT image with the corresponding SR image, absolute error map, uncertainty maps, and SSIM map are shown in Fig.7. As mentioned in the method section, out-of-distribution data can be identified with epistemic uncertainty but not with aleatoric uncertainty alone [30]. As shown in Fig.7D, the aleatoric uncertainty pervades over the whole image volume, including the background region, whereas the epistemic uncertainty map in Fig.7E shows significantly emphasized regions in specific anatomical structures. Furthermore, the regions with high values in the epistemic uncertainty map correspond to the regions with higher error in the absolute error map and lower SSIM in the SSIM map, and vice versa.

In addition, by investigating the relationships between the mean epistemic uncertainty of each image slice and their SSIM/PSNR values and observed strong correlations between them. As shown in Fig.8, we first performed linear regression on the pairs of mean epistemic and SSIM values using the 10 datasets from the test group (blue dots), and obtained a linear regression (the red solid line) with a 95% prediction interval (the region between the red dashed lines). Due to the logarithmic function of PSNR, an exponential regression was performed on the pairs of mean epistemic and PSNR values, and a regression equation with a 95% prediction interval was also obtained. The  $R^2$  values of the regressions were greater than 0.8, indicating that the regressions fit the data well. Then, we included 40 additional datasets, which were isolated from the training/validation/test groups, to validate the accuracy of the regressions in predicting the SSIM and PSNR from the mean epistemic uncertainty values. The additional 40 datasets are represented as green crosses in Fig.8 with approximately 95% of the data located in the prediction intervals for all regressions, indicating that the correlations between mean epistemic uncertainty and SSIM/PSNR closely follow the predicted distribution. Therefore, the proposed method can predict the SSIM and PSNR values when ground truth is not available in clinical settings.

#### IV. CONCLUSION

In this manuscript, we first proposed a method using T-RCAN network for the restoration of 3D high quality MR

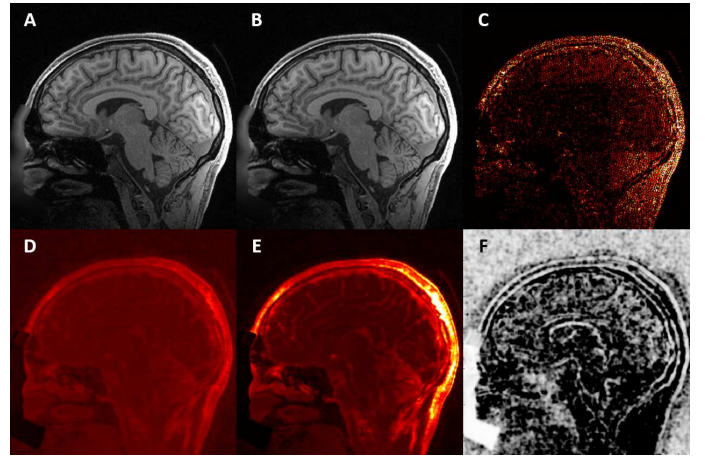


**Fig. 7:** Visual effect of aleatoric and epistemic uncertainty:  
A. high-resolution ground truth (HRGT) image; B. super-resolution (SR) image; C. absolute error between HRGT and SR images; D. aleatoric uncertainty map; E. epistemic uncertainty map; F. SSIM map.

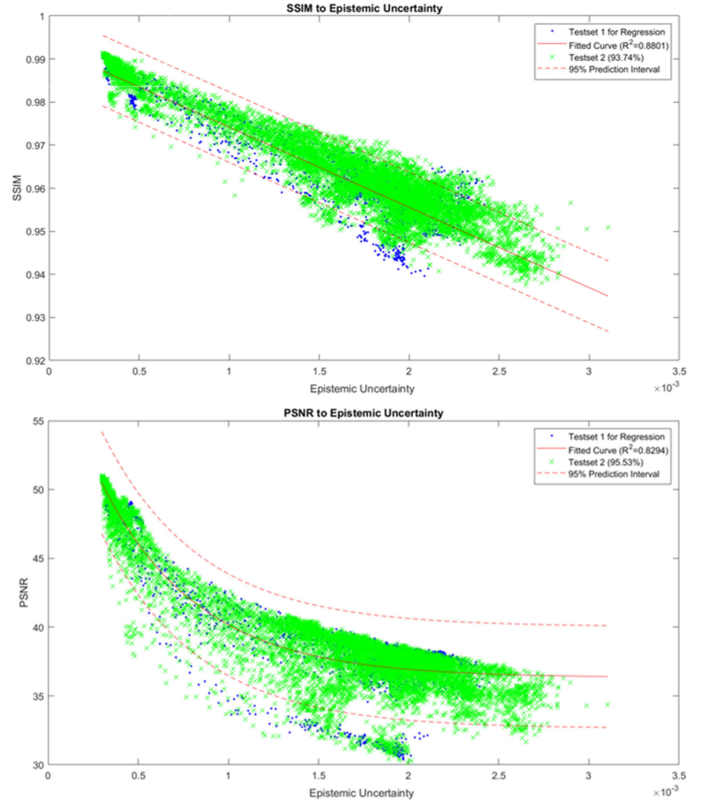


**Fig. 8:** Regression of SSIM/PSNR to epistemic uncertainty.

images. In the SR task, our network outperformed 3D networks in all downsampling strategies, while consuming down to 10.4% of GPU resources and less than 25.5% of inference time compared to mDCSRN, indicating that it can be easily deployed on any consumer GPU. In the MAR task, our network in 2D mode performed significantly better than the UNet, and it further improved its performance in 3D mode by enhancing through-slice agreement. Besides, our method can be extended by using a 3D network to process 4D images, for instance, enhancing temporal and spatial resolutions simultaneously.

In addition, we compared various combinations of in-plane and through-plane dwonsampling with different scale factors. Our experiments revealed that using  $1 \times 1 \times 2$  for  $\times 2$  acceleration and  $2 \times 2 \times 2$  for  $\times 4$  acceleration results in the best SR reconstruction performance. Therefore, these down-sampling strategies are recommended for acquiring real LR images when applying deep learning-based SR reconstruction in clinical environment.

Furthermore, we proposed a novel method for retrospective motion artifact generation. A predefined motion pattern with adjustable duration and frequency of movement was used in our method, resulting in controllable and quantifiable severity of the generated motion artifacts. Motion artifacts corrupted images with linearly increased SSIM and PSNR values were obtained by varying the frequency of movement in our experiments. The motion pattern can be adjusted based on any specific scenario.

Finally, we used evidential regression learning to generate uncertainty maps using our network simultaneously with the reconstructed images. The generated epistemic uncertainty map corresponded to the absolute error and SSIM map between the ground truth and the reconstructed image. In addition, we investigated the relationship between epistemic uncertainty and the SSIM/PSNR values. Our experiments revealed that the mean uncertainty of each image slice was linearly and exponentially related to the SSIM and PSNR, respectively. Therefore, when ground truth is not available in clinical settings, the SSIM and PSNR values can be predicted using the regression equations derived from pairs of images from the test dataset.

## REFERENCES

- [1] Dong, C., Loy, C.C., He, K., Tang, X., 2016. Image super-resolution using deep convolutional networks. *IEEE transactions on pattern analysis and machine intelligence* 38, 295-307.
- [2] Dong, C., Loy, C.C., Tang, X., 2016. Accelerating the super-resolution convolutional neural network, in: *European Conference on Computer Vision*, Springer. pp. 391-407.
- [3] Sun, S., Chen, W., Wang, L., Liu, X., Liu, T.Y., 2016. On the depth of deep neural networks: A theoretical view., in: *AAAI*, pp. 2066-2072.
- [4] Glorot, X., Bengio, Y. Understanding the difficulty of training deep feed-forward neural networks, in: *Proceedings of the Thirteenth International Conference on Artificial Intelligence and Statistics* 2010, 249-256.
- [5] Kaiming He, Xiangyu Zhang, Shaoqing Ren, Jian Sun: Deep Residual Learning for Image Recognition. *IEEE Conference on Computer Vision and Pattern Recognition (CVPR)*, 2016.
- [6] Yulun Zhang, Kunpeng Li, Kai Li, Lichen Wang, Bineng Zhong, Yun Fu; Proceedings of the European Conference on Computer Vision (ECCV), 2018, pp. 286-301.
- [7] Litjens, G., Kooi, T., Bejnordi, B.E., Setio, A.A.A., Ciompi, F., Ghafoorian, M., van der Laak, J.A., van Ginneken, B., Sanchez, C.I. A survey on deep learning in medical image analysis. *Medical image analysis* 2017 42, 60-88.
- [8] Oktay, O., Bai, W., Lee, M., Guerrero, R., Kamnitsas, K., Caballero, J., de Marvao, A., Cook, S., ORegan, D., Rueckert, D., 2016. Multi-input cardiac image super-resolution using convolutional neural networks, in: *International Conference on Medical Image Computing and Computer-Assisted Intervention*, Springer. pp. 246-254.
- [9] You, C., Li, G., Zhang, Y., Zhang, X., Shan, H., Li, M., Ju, S., Zhao, Z., Zhang, Z., Cong, W., et al., 2019. CT super-resolution GAN constrained by the identical, residual, and cycle learning ensemble (GAN-CIRCLE). *IEEE Transactions on Medical Imaging* 39, 188-203.
- [10] Wang, S., Su, Z., Ying, L., Peng, X., Zhu, S., Liang, F., Feng, D., Liang, D., 2016. Accelerating magnetic resonance imaging via deep learning, in: *Biomedical Imaging (ISBI), 2016 IEEE 13th International Symposium on*, IEEE. pp. 514-517.
- [11] Chen, Y et al. Brain MRI Super Resolution Using 3D Deep Densely Connected Neural Networks. 2018 IEEE 15th International Symposium on Biomedical Imaging.
- [12] Chen, Y et al. Efficient and Accurate MRI Super-Resolution using a Generative Adversarial Network and 3D Multi-Level Densely Connected Network, 2018 MICCAI, pp. 91- 99.
- [13] Pham, C.H., Ducournau, A., Fablet, R., Rousseau, F., 2017. Brain MRI super resolution using deep 3D convolutional networks, in: *Biomedical Imaging (ISBI 2017)*, 2017 IEEE 14th International Symposium on, IEEE. pp. 197-200.
- [14] Xiaole Zhao, Yulun Zhang, Tao Zhang, and Xueming Zou. Channel Splitting Network for Single MR Image Super-Resolution. *IEEE TRANSACTIONS ON IMAGE PROCESSING* 2019, 28, 5649-5662.
- [15] Pham C H, Tor-Diez C, Meunier H, et al. Multiscale brain MRI super-resolution using deep 3D convolutional networks. *Computerized Medical Imaging and Graphics*, 2019, 77: 101647.
- [16] Evan M. Masutani, Naeim Bahrami, Albert Hsiao. Deep Learning Single-Frame and Multiframe Super-Resolution for Cardiac MRI. *Radiology* 2020; 295:
- [17] Akshay S. Chaudhari, Zhongnan Fang, Feliks Kogan, Jeff Wood, Kathryn J. Stevens, Eric K. Gibbons, Jin Hyung Lee, Garry E. Gold, Brian A. Hargreaves. Super-resolution musculoskeletal MRI using deep learning. *Magn Reson Med* 2018; 80: 2139-2154.
- [18] ZHANG SIYUAN, DONG JINGXIAN, JIANG CAIWEN, HOU WEN-GUANG, DENG XIANBO. 2D CNN-Based Slices-to-Volume Superresolution Reconstruction. *IEEE Access* 2020, 8, 86357-86366.
- [19] Wei Lu, Zhijin Song, Jinghui Chu. A novel 3D medical image super-resolution method based on densely connected network. *Biomedical Signal Processing and Control* 2020, 62, 102120.
- [20] Küstner T, Armanious K, Yang J, Yang B, Schick F, Gatidis S. Retrospective Correction of Motion-affected MR Images using Deep Learning Frameworks. *Magn Reson Med* 2019; 82: 1527-1540.
- [21] Johnson PM, Drangova M. Conditional generative adversarial network for 3D rigid-body motion correction in MRI. *Magn Reson Med* 2019; 82: 901-910.
- [22] Chunga, H et al.. Simultaneous super-resolution and motion artifact removal in diffusion-weighted MRI using unsupervised deep learning. *arXiv:2105.00240v1*
- [23] Chengyan Wang, Yucheng Liang, Yuan Wu, Siwei Zhao, Yiping P. Du. Correction of out-of-FOV motion artifacts using convolutional neural network. *Magnetic Resonance Imaging* 2020, 71, 93-102.
- [24] Ben A Duffy, Lu Zhao, Farshid Sepehrband, Joyce Min, Danny JJ Wang, Yonggang Shi, Arthur W Toga, Hosung Kim. Retrospective motion artifact correction of structural MR images using deep learning improves the quality of cortical surface reconstructions. *NeuroImage* 230 (2021) 117756.
- [25] Gyutaek Oh, Jeong Eun Lee, and Jong Chul Ye. Unpaired MR Motion Artifact Deep Learning Using Outlier-Rejecting Bootstrap Aggregation. *IEEE TMI*.2021.3089708.
- [26] Seul Lee, Soozy Jung, Kyu-Jin Jung, Dong-Hyun Kim. Deep Learning in MR Motion Correction: a Brief Review and a New Motion Simulation Tool (view2Dmotion). *iMRI* 2020;24:196-206.
- [27] Ryutaro Tanno, Daniel E. Worrall, Enrico Kaden, Aurobrata Ghosh, Francesco Grussu, Alberto Bazzi, Stamatios N. Sotiropoulos, Antonio Criminisi, Daniel C. Alexander. Uncertainty Quantification in Deep Learning for Safer Neuroimage Enhancement. *arXiv:1907.13418v1*.
- [28] Yu Qin, Zhiwen Liu, Chenghao Liu, Yuxing Li, Xiangzhu Zeng, Chuyang Ye. Super-Resolved q -Space deep learning with uncertainty quantification. *Medical Image Analysis* 2021; 67: 101885.
- [29] Balaji Lakshminarayanan, Alexander Pritzel, Charles Blundell. Simple and Scalable Predictive Uncertainty Estimation using Deep Ensembles. *NIPS* 2017.
- [30] Alex Kendall, Yarin Gal. What Uncertainties Do We Need in Bayesian Deep Learning for Computer Vision? *NIPS* 2017.

- [31] Alexander Amini, Wilko Schwarting, Ava Soleimany, Daniela Rus. Deep Evidential Regression. NeurIPS 2020.
- [32] Hang Zhao, Orazio Gallo, Iuri Frosio, and Jan Kautz: Loss Functions for Image Restoration With Neural Networks. IEEE Transactions on Computational Imaging, 2017.
- [33] Barron JT, A General and Adaptive Robust Loss Function. arXiv:1701.03077.
- [34] Zhou Wang, Alan C. Bovik, Hamid R. Sheikh, Eero P. Simoncelli: Image Quality Assessment: From Error Visibility to Structural Similarity. IEEE Transactions on Image Processing, 2004.
- [35] Evan M. Masutani, Naeim Bahrami, Albert Hsiao. Deep Learning Single-Frame and Multiframe Super-Resolution for Cardiac MRI. Radiology 2020; 295:
- [36] Van Essen, D.C., Smith, S.M., Barch, D.M., Behrens, T.E., Yacoub, E., Ugurbil, K., Consortium, W.M.H., et al., 2013. The WU-Minn human connectome project: an overview. Neuroimage 80, 62-79.
- [37] Dong C, Loy C C, He K, et al. Image super-resolution using deep convolutional networks. IEEE transactions on pattern analysis and machine intelligence, 2015, 38(2): 295-307.
- [38] C. Dong, C. C. Loy, and X. Tang, “Accelerating the super-resolution convolutional neural network,” in Proc. Eur. Conf. Comput. Vis., 2016, pp. 391–407